

Geochemistry, Geophysics, Geosystems

RESEARCH ARTICLE

10.1029/2020GC009024

Special Section:

Tethyan dynamics: from rifting to collision

Key Points:

- A crustal Vs model is presented using ambient noise and transdimensional tomography to image the Paleo-Tethys closure in south-east China
- Distinct crustal velocity domains are linked to Precambrian terranes, slow suture/fault zones, and fast Dabie-Sulu orogenic crust
- Crustal detachment faults and lithospheric wedge across the Tanlu Fault favor a northward subduction of the Yangtze lithosphere

Supporting Information:

- Supporting Information S1

Correspondence to:

H. Yuan,
huaiyu.yuan@gmail.com

Citation:






T. Li, L. Zhao, B. Wan, Z.-X. Li, T. Bodin, & K. Wang, et al. (2020). New crustal Vs model along an array in south-east China: Seismic characters and Paleo-Tethys continental amalgamation. *Geochemistry, Geophysics, Geosystems*, 21, e2020GC009024. <https://doi.org/10.1029/2020GC009024>

Received 9 MAR 2020

Accepted 11 JUN 2020

Accepted article online 13 JUN 2020

New Crustal Vs Model Along an Array in South-East China: Seismic Characters and Paleo-Tethys Continental Amalgamation

Tingzi Li^{1,2,3,4}, Liang Zhao^{1,2} , Bo Wan^{1,2} , Zheng-Xiang Li⁵ , Thomas Bodin⁶ , Kun Wang¹, and Huaiyu Yuan^{3,4} 

¹State Key Laboratory of Lithospheric Evolution, Institute of Geology and Geophysics, Chinese Academy of Sciences, Beijing, China, ²University of Chinese Academy of Sciences, Beijing, China, ³ARC Centre of Excellence for Core to Crust Fluid Systems, Department of Earth and Environmental Sciences, Macquarie University, North Ryde, NSW, Australia, ⁴Centre for Exploration Targeting, University of Western Australia, Crawley, WA, Australia, ⁵Earth Dynamics Research Group, ARC Centre of Excellence for Core to Crust Fluid Systems and the Institute for Geoscience Research, School of Earth and Planetary Sciences, Curtin University, Perth, WA, Australia, ⁶Université Lyon, Université Lyon 1, Ens de Lyon, CNRS, Lyon, France

Abstract The assembly of East Asia was closely linked to the closure of the Tethyan oceans. In south-east China, the closure of the Paleo-Tethys ocean led to a continental collision between the South China and North China blocks (SCB and NCB), forming the world renowned (ultra-) high pressure (UHP) metamorphic belt of the Dabie-Sulu Orogen. The region was subsequently reworked by postorogenic extensional processes. These tectonic processes likely have left lithospheric scars identifiable by seismic imaging techniques. Here we characterize seismic structures across the orogen and analyze processes related to the closure of the Paleo-Tethys. Using cutting-edge tomographic approaches and ambient noise dispersion data, we developed a fine-scale crustal shear-wave velocity model beneath key crustal domains in the region. Distinct crustal scale velocity domains are identified, corresponding to the normal Precambrian crust, slow-velocity suture zones and fault systems, and fast-velocity orogens, suggesting a deep root of the corresponding surface geological features. By combining recent models of active-source, gravity and magnetotellurics, characteristic lithospheric deformation patterns such as crustal thrust systems and lithospheric wedges can be inferred, which are attributed to a northward subduction of the SCB lithosphere and the eventual continental collision after the closure of the Paleo-Tethys Ocean.

1. Introduction

The assembly of East Asia involved numerous continental collisions (e.g., Li, 1998; Stern et al., 2018; Zheng et al., 2013; Zhao et al., 2018). In south-east China, from north to south, the major tectonic units include the Neoproterozoic to Paleozoic Central Asian Orogenic Belt (CAOB), the Archean-Proterozoic North China Block (NCB), the Paleozoic–Mesozoic Sulu-Dabie Orogen (SDO), and the Archean–Proterozoic South China Block (SCB) (Figure 1; Li, 1998; Stern et al., 2018; Zheng et al., 2013). The Paleozoic–Mesozoic orogens recorded successive closure of Proto- and Paleo-Tethys Oceans, and the docking of continental blocks or terranes from Gondwana to the margin of Eurasia (e.g., Cawood et al., 2009; Metcalfe, 2013; Sengor et al., 1993; Zhao et al., 2018; Zheng et al., 2013). The progressive collisional events have left a rich tectonic archive of geological, geochemical, and geophysical records (e.g., Cawood et al., 2018; Metcalfe, 2013), making the region an ideal natural laboratory for investigating not only the amalgamation and evolution of continental blocks in south-east China but also mantle dynamics responsible for the one-way migration of Gondwana-originated terranes that are unique in the Tethyan evolution (Şengör, 1990; Wan et al., 2019).

A fundamental scientific goal of the Tethys Geodynamic Project is to understand the dynamics associated with continuous northward docking of Gondwana-originated terranes (e.g., Stampfli et al., 2013; Wan et al., 2019). From a deep seismological perspective, rifting and collisional events may work on the lithosphere and leave long-lived lithospheric marks or “scars” (e.g., Heron et al., 2016; Snyder, 2002; van der Velden & Cook, 2005). These scars may be characteristic to different tectonic processes (e.g., Clerc et al., 2018; Peron-Pinvidic et al., 2019) and can thus provide direct lithospheric records for such processes. Combined with surface geological and shallow geophysical observations, information obtained through deep seismic

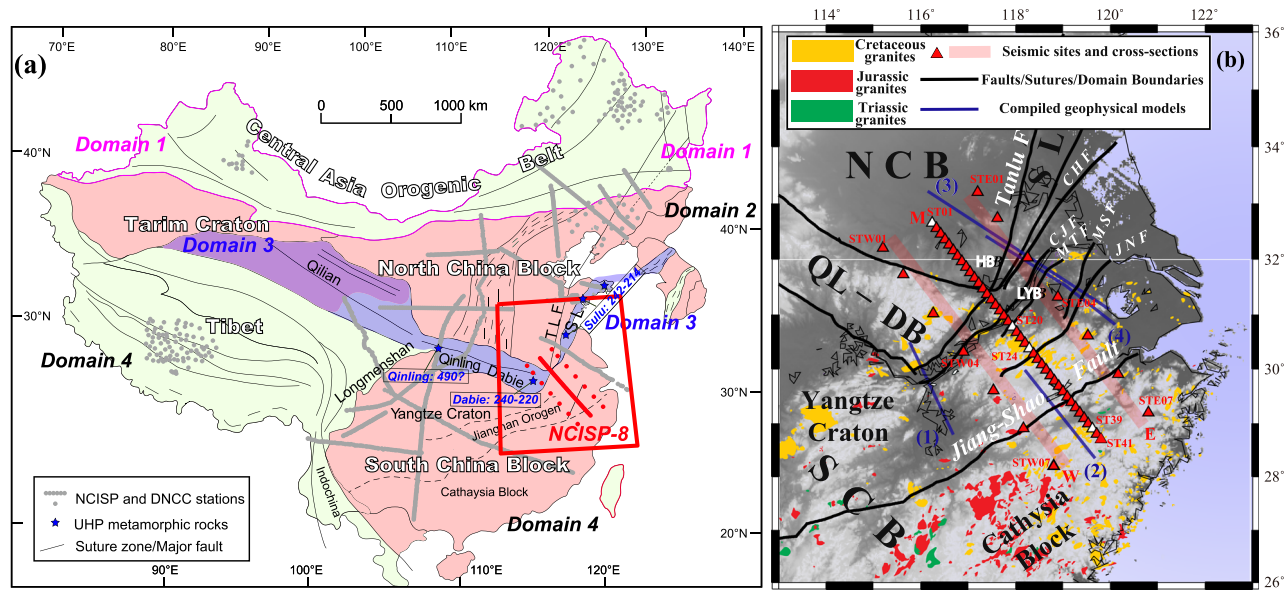


Figure 1. Tectonic setting and locations of geophysical transacts. (a) Major crustal domains of China and relationships with the Tethys tectonic domains, modified from Stern et al. (2018). The crustal domains are closely related to closure of Tethys Oceans: e.g., Domains 1 and 3 recorded the closure of both Proto-Tethys and a branch of Paleo-Tethys; Domain 4; the Neo-Tethys. Stars in Domain 3 show locations of UHP rocks. See Stern et al. (2018) for details. Gray lines and dots show the NCISP and DNCC arrays (see text). TLF—Tanlu Fault. SL—Sulu Orogen. (b) Regional tectonic map showing the tectonic domains, the NCISP-8 seismic arrays (red), compiled geophysical model locations (blue lines) and post-orogenic magmatism (red and green shaded regions) after the NCB-SCB continental collision. NCB—North China Block/Craton; QL-DB—Qinling-Dabie Orogenic Belt; SL—Sulu Orogenic Belt; HB—Hefei Basin; LYB—Lower Yangtze Basin. Local fault systems as in Lü et al. (2015): CJF—Yangtze Fault; MTF—Main Thrust Fault; JNF—Jiangnan Fault; MSF—east Maoshan Fault; and CHF—Chuhe Fault.

profiling may enable us to image such lithospheric scars and analyze the dynamics of orogens (e.g., Clerc et al., 2018; Thybo & Artemieva, 2013; van der Velden & Cook, 2005). One assumption for such an approach is that the scars have not been severely perturbed by subsequent tectonic reworking. In addition, deep structural imaging only provides a snapshot of the present-day lithospheric architecture. Therefore, cross-discipline considerations are usually needed to better interpret the structural features in terms of tectonic processes through time.

As part of the Tethys Geodynamics Project, a large-scale seismic imaging project was initiated through which high-density arrays (gray lines in Figure 1a) in China are compiled and remapped to characterize the seismic structures of the lithosphere. These arrays were deployed over the past decades as parts of two major imaging projects, the North China Interior Structure Project (NCISP) and the Destruction of the North China Craton (DNCC) projects to image the internal structures of the lithosphere with a focus on the destruction of the NCB (Zhao et al., 2012; Zheng et al., 2017; Zhu et al., 2011). These arrays covered major structural boundaries between the Proto- and Paleo-Tethys domains (Figure 1a; e.g., Stern et al., 2018), thus provide a unique opportunity to map out the shape, morphology, and composition of the Tethyan orogens in the region.

In this study, we target the ~500 km-long NCISP-8 deployment (red stations in Figure 1) in south-east China for its shallow lithospheric shear-wave structure. The area recorded major continental collisions after the closure of Paleo-Tethys Oceans, followed by subsequent intracontinental extension related to the western Pacific subduction since the Mesozoic. Earlier seismic studies using the NCISP-8 data set focused on the lithospheric architecture of the cratonic interior and interaction of the western Pacific subduction with the regional lithosphere, respectively (Wu et al., 2018; Zhao, Zheng, et al., 2013; Zheng et al., 2014). Here we attempt to link potential whole-crust and shallow lithospheric shear-wave structures with deep deformation processes during the continental collisions after the Paleo-Tethyan closure.

Using a two-step Bayesian transdimensional inversion techniques (Bodin & Sambridge, 2009; Bodin et al., 2012; see section 3 below), we developed a high-resolution probabilistic shear-wave crustal velocity model beneath the NCISP-8 array. The Rayleigh wave dispersion data set was acquired using the ambient

noise technique (Campillo & Paul, 2003; Shapiro & Campillo, 2004), which has become widely adapted for imaging fine-scale crustal structures (e.g., Bensen et al., 2007; Lin et al., 2013; Luo et al., 2019; Yang et al., 2012; Yao et al., 2006; Young et al., 2013; Zhao et al., 2020). In section 2 below, we provide a brief overview of the regional tectonics with emphasis on the Tethys tectonic domains. Section 3 presents seismic data preparation and tomographic inversion procedures. This is followed by our new crustal shear-wave velocity model, and in combination with previously published geophysical constraints, we discuss the lithospheric architecture in relation to continent-continent collision between the NCB and SCB (Figure 1) resulted from the Paleo-Tethys closure.

2. Regional Tectonics

Connecting the NCB and the SCB, the NCISP-8 seismic array straddles from the NCB, crossing the Qinling-Dabie-Sulu orogenic belt, into the SCB (Figure 1a). Preserving the oldest (~3.8 Ga) rocks in China (Liu et al., 1992), the NCB is dominated by Neoproterozoic to Paleoproterozoic basement, covered by younger sedimentary rocks. The NCB consists of the eastern and western blocks that assembled into a stable craton by around ~1.8 Ga along the Central Orogenic Belt (e.g., Zhao & Cawood, 2012; Zheng et al., 2013). After cratonization, the NCB has experienced several episodes of tectonic events, such as extension in the Paleoproterozoic during the breakup of the supercontinent Nuna (e.g., Zhao & Cawood, 2012) or during the Neoproterozoic (Wan et al., 2018), collision with the CAOB resulting from the closure of the Proto-Tethys (Domain 1 in Figure 1a) in the Permian (Xiao et al., 2013), and collision with the SCB and Tibetan terranes (Domain 4 in Figure 1a) since the Triassic.

The SCB consists of the Yangtze Craton and the Cathaysia Block. The Yangtze Craton includes an Archean–Paleoproterozoic crystalline basement and supracrustal assemblages. The Cathaysia Block consists of a Paleoproterozoic (Yu et al., 2009) and Mesoproterozoic (Li et al., 2008) metamorphic basement. The two blocks collided during late Mesoproterozoic to earliest Neoproterozoic (e.g., Li et al., 2009), followed by a widespread mid-Neoproterozoic rifting event (Li et al., 1999, 2003). The SCB also experienced lower Paleozoic (Li et al., 2010) and Mesozoic (Li & Li, 2007) tectonic reworking.

With the closure of a branch of the Paleo-Tethys in the Triassic, the SCB and the NCB collided along the Qinling-Dabie-Sulu Orogenic Belt (Domain 3 in Figure 1a; e.g., Hacker et al., 2006; Li, 1998; Meng & Zhang, 2000). Faults and shear zones in the orogenic belt are widely developed, associated with intensive metamorphism (Wang, Fan, et al., 2013), including the occurrence of ultrahigh pressure (UHP) metamorphism (blue stars in Figure 1a; Okay & Şengör, 1992; Xu et al., 1992). The orogenic belt is dissected by the Tanlu Fault, a large-scale left-lateral transform fault with the maximum translation distance of either ~110 km (Li, 1994) or ~500 km (Xu et al., 1987).

Since the late Mesozoic, both the NCB and the SCB have been involved in the Western (Paleo-) Pacific subduction system which resulted in wide-spreading magmatic activities (e.g., Li & Li, 2007; Stern et al., 2018). Multidisciplinary evidence suggested that part of the stable NCB was thinned due to the subduction of the Pacific Plate (Menzies & Xu, 1998; Wu et al., 2019; Zhu et al., 2011, 2012). Geophysical surveys also suggest thinning of the SCB lithosphere since the late Mesozoic (e.g., Li et al., 2015; Zheng et al., 2015; Zhou et al., 2012), characterized by lithospheric extension and widespread faulted basins and igneous rocks (e.g., Zheng et al., 2013). Jurassic-Cretaceous magmatism is widespread over much of the coastal zone of East China (Wu et al., 2005).

The multiple episodes of tectonic and magmatic events in southeastern China would have left distinct lithospheric structures, rendering an excellent research opportunity for deep seismic imaging.

3. Ambient Noise Data Processing and Tomographic Inversions

3.1. Ambient Noise Data

Waveforms used in this study span from October 2008 to April 2010, as part of the North China Interior Structure Project (NCISP-8). The array (Figure 1b) spreads nearly 500 km across the NCB, the SCB, and major faults in the region. It included 55 temporary stations, in which 41 stations were deployed on the main line with an average spacing of 10–15 km, and seven stations on each of the southwest and northeast auxiliary lines, respectively, with a larger spacing of 60–100 km. The instruments deployed in the array were

mostly 60-s Guralp CMG-3ESP broadband sensors combined with REF Tek 130s seismic recorders. A total of 65 sets of sensors were used over the course of the field deployment, during which 16 sets of 30 s CMG-3ESPs were swapped in to replace malfunctioned sensors during field services.

In the ambient noise processing, we followed the steps described in Yuan and Bodin (2018). Firstly, 100 Hz continuous vertical-component waveforms were downsampled to 5 Hz, and at the meantime, the instrument response was removed for both the 60 and 30 s sensors. We kept a flat response between 50 s and 5 Hz afterwards and cut data into 20-min long (with 20% overlapping) window. Each waveform window was further demeaned and detrended. Simultaneous waveforms of each station pair (in a total of 1,482 usable pairs) were computed to generate the cross-correlation functions (CCFs) to approximate Green's function (shared online at Open Science Foundation; see Data Availability Statement).

We avoided applying some conventional procedures used in other ambient noise studies (e.g., spectral whitening, one-bit normalization and temporal normalization) to obtain the CCFs, except that each CCF was amplitude-normalized to minimize effects of large amplitude earthquakes. In addition, a bootstrap procedure (Efron & Tibshirani, 1986) was applied to improve signal-to-noise ratio (SNR). One-hundred sets of randomly (with replacement) selected waveforms were generated and stacked. Each of the resampled waveform sets was composed of the same number of total available CCFs for the station pair. The average of the stacked CCFs of these 100 sets was taken as the final CCF and the standard deviation as the data error. This procedure empirically helps to further alleviate effects of large waveform amplitudes from earthquakes, as well as temporal variations in noise sources (e.g., Stachnik et al., 2008; Yuan & Bodin, 2018).

In theory, Green's function consists of two symmetric branches, but due to uneven distribution of noise sources, the amplitudes and phases of the positive and negative branches may vary. Figure 2a shows an example of the CCFs between station ST01 and the other stations in vertical component, suggesting that the signals come principally from the west of the Pacific Ocean. We averaged the two branches to form the final CCF used for dispersion measurements. The group velocity dispersion curves were measured through the Automatic Frequency-Time Analysis method (AFTAN; Levshin et al., 1972). After a band-pass filter of 0.015–2 Hz, we picked up dispersion curves with the constraints that the distance between the stations is greater than 2 times the wavelength and the SNR (determined by AFTAN) is larger than 20. We further removed the measurements with RMS value greater than twice the standard deviation. Finally, we acquired the group velocity dispersion curves of period ranging from 2.5 to 46 s for the group velocity tomography. Figure 2b shows examples of dispersion measurements between stations pairs that sample the north, south, and whole portions of the Main line. Figure 2c shows the number of available dispersion data for each period, and Figure 2d is the average of the dispersion measurements for the whole array and the standard deviation.

3.2. Dispersion Inversion and Resolution Tests

We applied a two-step inversion process to invert surface wave dispersion measurements for the 3-D crustal velocity model. The inversion includes (1) 2-D inversions at individual periods to obtain group dispersion maps and (2) 1-D inversions at model grid points, which are then combined to form the final 3-D shear wave velocity model. There are recent improvements of more sophisticated one-step inversions that invert directly frequency-dependent dispersion data into 3-D structure (e.g., Fang et al., 2015; Zhang et al., 2018). This two-step procedure is based on fully nonlinear Monte-Carlo inversions where the forward modeling does not need to be linearized around a reference model, and no derivatives and kernels are needed. In addition, no subjective damping and regularization parameters are needed (Bodin et al., 2012; Bodin & Sambridge, 2009).

In the first step of the procedure, we inverted travel times of Rayleigh waves measured between pair of stations to produce 2-D map of group velocities. This 2-D tomography was carried out independently at each period. For that, we applied a two-dimensional reversible jump tomographic method (Bodin & Sambridge, 2009). The velocity model was parameterized with Voronoi cells with mobile geometry and number. The size, position, and shape of the cells, as well as velocities in each cell were unknown parameters to be determined by the data. The inversion was cast in a Bayesian framework, and many velocity models were sampled with a transdimensional Markov chain algorithm. Information extracted from the whole

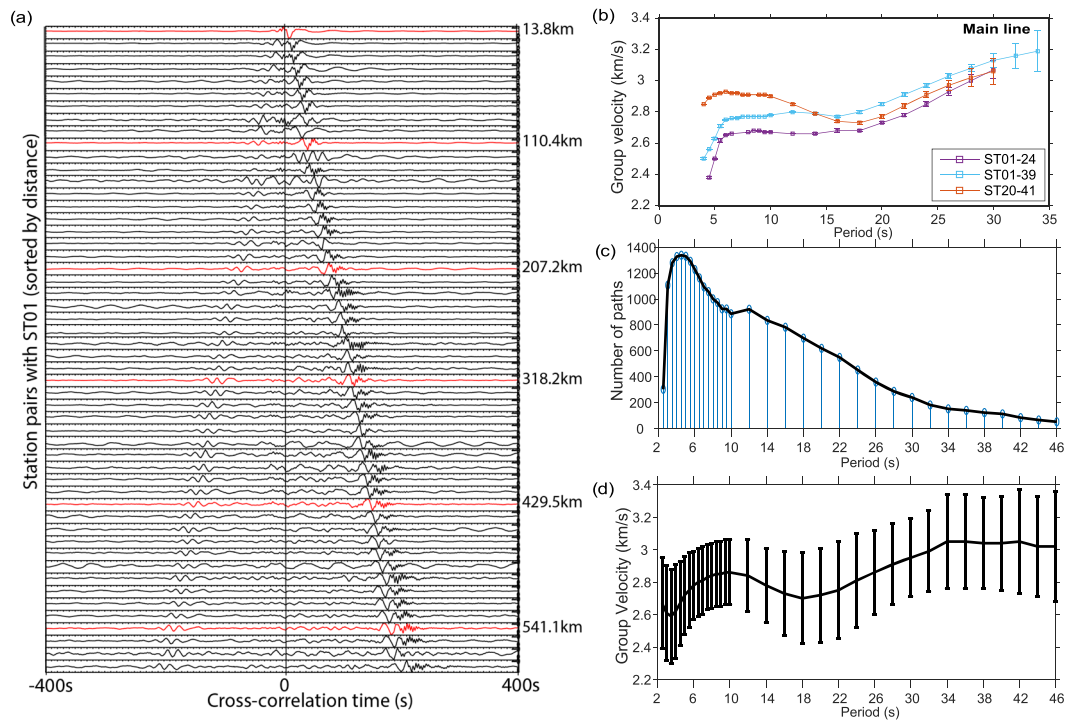


Figure 2. Examples for ambient noise data processing. (a) Vertical channel cross-correlation between ST01 and the other stations. (b) Dispersion measurements for three paths. Stations are marked in the Figure 1b by white triangles. Note the relatively slow group velocities above 20 s for the northern half of the array (ST01–24), indicating a slow upper- to mid-crust, while the southern half of the array (ST24–41) is fast. Note that the example station pairs do not necessarily have measurements up to 46 s subject to data culling criteria. (c) Number of measurements for all periods (2.5–46 s), which is the data period range for velocity inversion. (d) The regional average group velocity with errors for all paths.

ensemble solution was used to generate the average model and model uncertainties. Readers are referred to the original method paper (Bodin & Sambridge, 2009).

There were two loops during this 2-D tomography. In the outer loop, the fast-marching method of Rawlinson and Sambridge (2005) was applied to obtain ray paths geometries for a reference model. The inner loop is a Markov chain, where at each step, a new velocity field (parameterized in terms of Voronoi cells) is randomly proposed, the level of data fit is computed, and the proposed model is either accepted or rejected according to the following acceptance rule given by the Metropolis algorithm: If the proposed model fits better the data, it is accepted. Otherwise, the proposed model is randomly accepted with probability equal to the ratio of misfits between the proposed and current model (Chib & Greenberg, 1995).

The ensemble of collected models was asymptotically distributed according to the posterior probability distribution. For each iteration of the outer loop, a reference smooth model was generated by simply averaging the ensemble of accepted Voronoi models in inner loop. We then used this smooth velocity model to update the raypaths using the fast-marching method for the next iteration. This approach therefore avoids the choice for subjective model parameterization and damping, which are typical in traditional inversion problems. Readers are referred to the original papers for more details (Bodin & Sambridge, 2009).

This 2-D tomography was carried out in the whole 2-D region that defined from 28°N to 34°N in latitude and from 115°E to 121°E in longitude with 60 × 60 grid points. After the inversion for each period, the inverted group velocity model was assembled for all periods and sorted for the depth inversion (section 3.3). In the computation processes, we used 144 CPUs, and 60,000 (20,000 burn-in steps and 40,000 more samples) models were computed by each CPU. The inversion time for each period was determined by the number of raypaths. We obtained the final group velocity model after three iterations. Figure S1 in the supporting information shows the distribution of stations and interstation raypaths and inverted group velocity maps for representative periods.

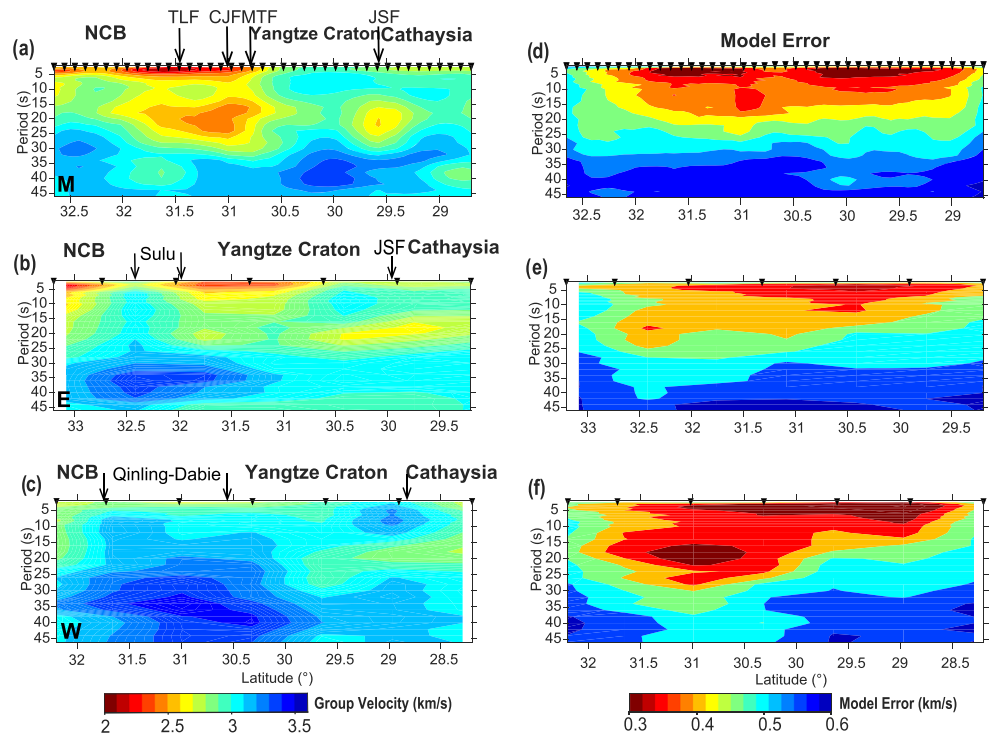


Figure 3. Group velocity inversion results plotted along the three lines: (a) to (c), the main line, east line and west line, respectively; (d) to (f), the model uncertainty from the 2-D *rj_McMC* tomography. M, E, and W stand for Main, East and West lines. Note that for all lines, model errors are relatively small below 30 s. Locations of the lines can be found in Figure 1b.

Figure 3 shows the group velocity model along the three profiles. The Main line was selected along the central stations. Two auxiliary lines slightly off-axis were selected as East and West lines (see Figure 1b), so that more crossing rays can improve the resolution. Large lateral variations can be found in the group velocity model across major structural boundaries (indicated by arrows in Figure 3). The group velocity of the short period (about 2.5 to 10 s) is mainly influenced by the velocity structure of the upper and middle crust, especially the sedimentary basins. Along the main line there are low group velocity anomalies beneath the TLF and the northwestern part of the Yangtze craton, which spatially correspond to the shallow surface basins (the Hefei and Lower Yangtze basins; Figure 1b). The group velocity is relatively fast to the north and south. The 10–25 s velocities mainly reflect the structures of the middle and lower crust. As can be seen in Figure 3a, the slow velocity beneath the TLF extends further into both the NCB and the Yangtze Craton. A secondary slow group velocity structure can be found beneath the Jiangshao Fault (JSF) and the Cathaysia Block in all three lines (note the auxiliary lines have coarse spatial resolution owing to sparse station spacing; Figure S2). The results above 30 s are mainly affected by the lower crust and the top of the upper mantle in the study area, where our synthetic tests show lateral resolution may reach 0.4° to 0.6° (Figures 4 and S2). Fast group velocities are observed beneath the Yangtze Craton in the main line and beneath the Qinling-Dabie and the Sulu orogens in the auxiliary profiles.

Resolution tests were conducted to investigate the resolving capability of seismic data and to assess the coverage quality of ray path in the study area. Given the linear nature of our profiles, we used narrow banded stripes with alternating velocity perturbation of 0.4 km/s, that is, the mean velocity ± 0.4 km/s at each period (Figure 2d). Synthetic travel times were computed using the fast marching package with 2% noise added, and we ran the *rj_McMC* package in the similar way to retrieve the input structure. Figure 4 illustrates beneath the main line the resolvable synthetic structural sizes by our data at various periods: $\sim 0.4^\circ$, 0.6° , about 0.8° , and over $\sim 1^\circ$ for period under 26 s, 26 to 34 s, 34 to 40 s, and over 40 s, respectively. Across the two auxiliary lines, the resolution there is not ideal due to the sparse station spacing (Figure S2a), and we therefore only focus on large scale structure hereafter in.

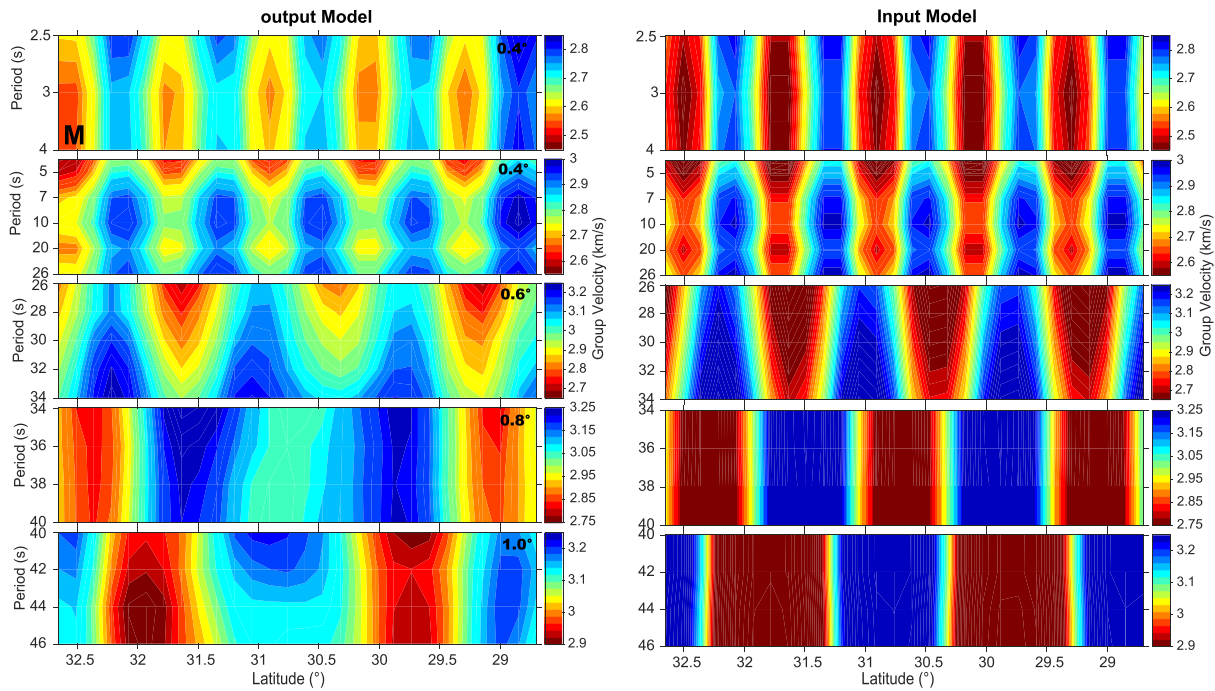


Figure 4. Resolution tests for resolvable structural size at selected periods. (a) Recovered models along the main line. Labels on the vertical axis show the periods tested. (b) Input models. Note the pattern of the input velocity structure is recovered well but the amplitude recovery is less satisfactory. More resolution test results are shown in Figure S2.

One advantage of the two-dimensional reversible jump tomography is that in generating the average model from the whole ensemble solution, the standard deviation of the models can be interpreted as an error map (Bodin & Sambridge, 2009). The model error plots in Figures 3 and S2e–S2g reflect a combination of different effects of ray path coverage, observational errors due to uneven noise source distribution, errors made in the forward theory, and the complexity of the underlying true model. These posterior uncertainties help us decide robust model areas for interpretation. Figure 3 shows that smaller model errors are usually present up to 30–35 s periods in all three profiles, suggesting robust model features are obtained by the inversion; while in the longest periods (>35 s), the model errors are considerably larger, which is consistent with fewer paths and increasing data errors at long periods (e.g., Figure 2d).

3.3. Transdimensional Inversion for 1-D Velocities

In the second step, we inverted at each geographical point the dispersion curve obtained in the first step to constrain a 1-D crustal shear wave velocity profile. As for 2-D tomography, we applied a transdimensional Bayesian inversion. The method treats the number of unknown parameters (here the number of layers) as unknown variables (Bodin et al., 2012). Here again, the Markov chain Monte Carlo (MCMC) method was implemented to generate a sequence of 1-D shear velocity models that are distributed according to the posterior distribution. The model $V_S(z)$ is defined by the perturbations $dV_S(z)$ around a reference model $V_S^0(z)$:

$$V_S(z) = V_S^0(z) (1 + dV_S(z)).$$

The reference model $V_S^0(z)$ was initially required to give physically meaningful bounds for the velocity variation or to impose discontinuities that remain fixed in the solution (e.g., Calò et al., 2016). A uniform priori distribution is often used where $dV_S(z)$ is the range of perturbations, $\pm 35\%$ of $V_S^0(z)$. Note that these perturbations do not need to set small, as there is no linearization involved here. Also note that our inversion relies on dispersion data from vertical component cross-correlation functions which are only sensitive to vertically polarized shear waves V_{sv} . For simplicity we discuss through the rest of the paper the velocity features as the V_S features; strictly speaking they should be V_{sv} features.

The structure of the crust may be highly complex, and it is often not trivial to find adequate prior models for some regions. Yuan and Bodin (2018) investigated to what extent different reference models $V_S^0(z)$ may affect the results and indicated that structures in the shallow crust may be recovered well independent of the different reference models. However, some amplitude mismatches are showed, especially in the lower crust. Yuan and Bodin (2018) concluded that having a robust reference model may help to give a better recovery in both the crustal velocities and the Moho topography than using the constant velocity crust reference model.

In this work, we used the smoothed model of Xin et al. (2018) as the 1-D reference model. The reference model considered here was developed using double-difference seismic travel-time tomography (Xin et al., 2018), and therefore is independent from our ambient noise dispersion dataset. We further tested a uniform prior model (3.9 km/s half space; see Figure S3a). Misfit comparison is shown in Figure S4a. In terms of that the optimization of the McMC sampler requires large computational resources for sufficient random walks, the final inversion was performed on a Cray Super computer (Magnus at the Pawsey Super Computing Centre, Western Australia) using 288 independent Markov chains/CPU's that sampled the model space simultaneously and independently. Each chain ran for 30,000 models (burn-in steps are 10,000 and then samples are 20,000). The result of the Bayesian transdimensional inversion is the posterior distribution drawn from the large ensemble of models. The posterior mean model is simply constructed by taking the average velocity at each depth across the whole ensemble posterior solution (e.g., Figures 5a, 6a, and 6c). The standard deviation can be used to indicate the level of uncertainty around the model. As Figures 5b, 6b, and 6d show that the model errors are in general small in the crust, except close to the surface where we may not have enough short period data (our dataset starts at 2.5 s). Below ~40 km, model errors increase rapidly, which are consistent with limited depth sensitivity (Figure S4b) carried by our data. We therefore confine our interpretations within the crust.

4. New Crustal Velocity Model and Tectonic Implications

The inverted crustal shear-wave velocity models along the three cross-sections are shown in Figures 5 and 6. Compared with available V_S models in this region (Figure S6), the new model has an improved lateral resolution in the crust due to the use of dense NCISP-8 stations. Several distinctive velocity domains are present (Figure 7), which are in a good accordance with surface geological features. In the framework of the Paleo-Tethys collision and the subsequent reworking of the regional lithosphere, we discuss the tectonic importance of these velocity features alongside other available geophysical observations (Table S1).

4.1. Feature 1—Precambrian Crust

Along the main profile major V_S features include: Feature 1 (F1.1 to F1.3) “normal” (i.e., close to the regional velocity average, black line in Figure 7) velocity blocks under the NCB (stations ST01 to ST08, F1.1 in Figure 5a), the southern YC (stations ST23 to ST30, F1.2) and the Cathaysia Block (south of station ST34, F1.3). These blocks have an overall increasing velocity trend from the upper crust to the Moho (Figures 7a–7c): A rapid velocity increase down to ~10 km, then a relatively constant (~3.4 km/s) velocity to ~20 km, and a gradual velocity increase across the Moho (~33 km according to Zheng et al., 2014).

Feature 1 spatially corresponds very well to the Precambrian basement. Several features corresponding to the basement crust are also reported in the region: a ~1.75 bulk crustal V_p/V_S ratio (He et al., 2014), close to the global continental average value (Christensen, 1996); an average Bouguer gravity anomaly (Figures S6c and S6e); and overall high crustal resistivities (Figure S6g; Zhang et al., 2019; also Zhang et al., 2015), suggesting dry continental crust (Jones, 2013).

4.2. Feature 2—Slow Velocity Mid-Crust Beneath the JSF

A mid-crustal slow velocity feature (Feature 2 in Figures 5 and 6; also and Figure 7d) is present beneath the major fault, the Jiangshao Fault (JSF) in the South China Block, which separates the Yangtze craton and the Cathaysia blocks (e.g., Zhao & Cawood, 2012). This slow velocity feature extends spatially beneath the two auxiliary lines (Figure 6), although the resolution of tomographic inversion there is much coarser (Figure S2). Previous crustal velocity studies along the main profile have found similar slow velocities beneath the JSF: receiver function inversion (Zheng et al., 2014) showed a slow velocity zone in the mid-crust to lower crust (>25 km depth); and surface wave inversions (Bao et al., 2015; Wu et al., 2018) also reported the similar slow velocity structure in the mid-crust beneath the JSF (Figures S5d and S5g).

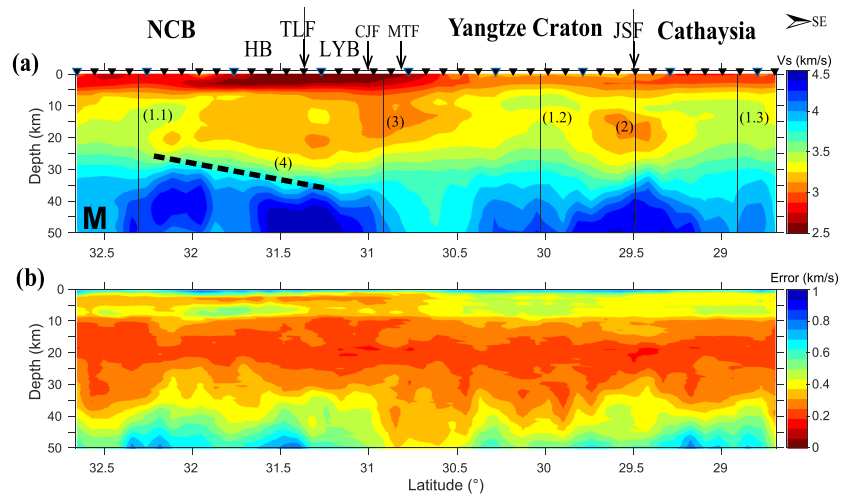


Figure 5. Transdimensional inversion results plotted along the main line. (a) The shear-wave velocity model. Numbers (1.1–1.3, 2–4), black dash line and vertical lines mark the velocity features discussed in the text, also in Figure 7. (b) The model error obtained from the transdimensional inversion. Note most of the velocity features reside in regions with relatively small model errors.

These features were formerly attributed to magmatic activities associated with the lithospheric modification related to the (paleo-) Pacific subduction. The very slow shear wave velocity (~ 3.2 km/s) could be consistent with the presence of melts in the crust. However, if melts are present, large (>2.0) V_p/V_s ratio would be expected (Christensen, 1996; Wang, Bagdassarov, et al., 2013). This is obvious not the case underneath the JSF because of small (~ 1.70) V_p/V_s ratios (Figure S6f) revealed in several studies (Guo et al., 2019; He et al., 2014; Li et al., 2018; Zhang et al., 2005; Zhang, Xu, et al., 2013). In addition, rather than yielding high conductivity for melts (Jones & Ferguson, 2001), the mid-crust beneath the JSF is resistive as indicated by magnetotelluric study (Figure S6g).

A felsic origin is likely to account for this slow mid-crust velocity feature beneath the JSF, consistent with wide-spreading Cretaceous granitic magma activities reported across the Cathaysia region (e.g., Gan et al., 2019). The very slow Vs velocity (~ 3.2 km/s) is somewhat slower than the laboratory measured values (>3.4 km/s; Christensen, 1996; Wang, Bagdassarov, et al., 2013). We suggest that high heat flow in the region (e.g., Figs. 6, 7 in Jiang et al., 2019) may have played a critical role in decreasing the velocity (Christensen,

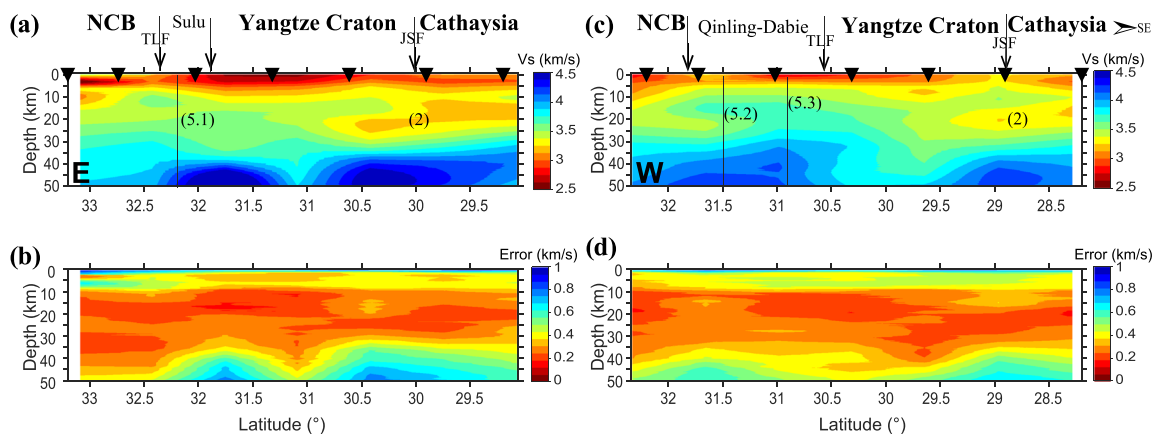


Figure 6. Transdimensional inversion results plotted along the two auxiliary lines: (a and b) the Vs model and model uncertainties along the east line; numbers (2, 5.1–5.3) and vertical lines indicate the velocity features discussed in the text, also in Figure 7; (c and d) the Vs model and model uncertainties along the west line.

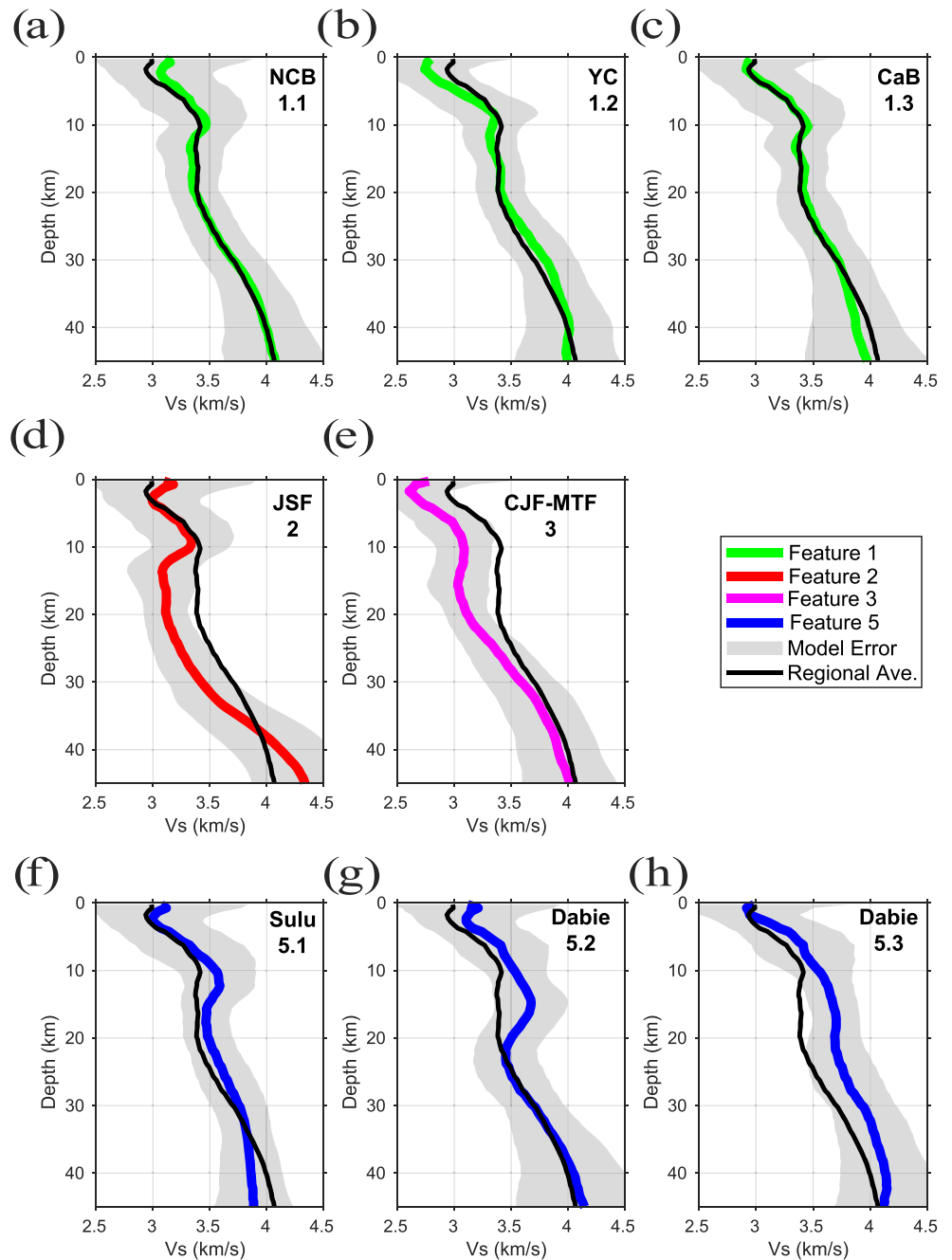


Figure 7. One-dimensional V_s profiles for the features discuss in the text: (a) to (c) the “normal” Precambrian crust whose velocity profiles are close to the regional average (black line); (d) and (e), the low velocity crust beneath the JSF and CJF-MTF systems; (f) to (h) high-velocity orogenic crust beneath the Sulu and Dabie Orogens.

and Mooney, 1995; see more discussion regarding the robustness and caveats in interpreting this feature in Text S2).

4.3. Feature 3—Slow Velocity Mid-Crust Beneath the CJF/MTF

There is a broad slow velocity zone in the shallow to mid-crust from 30.5°N to 32.0°N along the main profile (Figure 5). This feature spatially correlates to major fault systems the TLF, the Yangtze Fault (CJF), and the Main Thrust Fault (MTF) in the region. We interpret the TLF in section 4.4 below and only focus on the

feature beneath the CJF and the MTF (Feature 3 in Figure 5) where the velocity is slowest. These faults reside in one of the large metallogenic zones in eastern China (e.g., Lü et al., 2015; Luo et al., 2019).

A parallel high-resolution active source line lies about ~150 km northeast of the main line, and the inverted velocity model there shows two slow velocity structures underneath the TLF and the CJF/MTF systems. A gravity inversion also reveals two low density crustal columns beneath the two fault systems (Figure S6e). Unlike the slow crust of Feature 2, the whole crust V_p/V_s ratios here are measured relatively high (>1.75 in Guo et al., 2019; He et al., 2014; Li et al., 2018). This may rule out a felsic origin of the slow velocity feature here, but favors partial melting in the crust. In south-east China, various mantle processes are proposed to have reworked the lithosphere, including mantle plume, lithospheric delamination, magmatic underplating, and continental rifting (e.g., Jiang et al., 2019; Li & Li, 2007; Lü et al., 2015). Depressional melts triggered by these events may infiltrate the lithosphere especially in the structurally weak suture zones and large-scale faults, which eventually leads to concentration of ongoing melts in crust. The presence of melts is consistent with very high heat flow measurements, an average value of $74.2 \pm 14.8 \text{ mWm}^{-2}$ (Jiang et al., 2019) in the TLF system, and is favored by regional metallogenic models (e.g., Lü et al., 2015).

4.4. The Tanlu Fault Crust

The TLF is the largest strike-slip fault in eastern Asia (e.g., Zheng et al., 2013), which separated the Dabie Orogen from the Sulu Orogen (Figure 1). Among the three profiles (Figures 5a, 6a, and 6c), the whole-crust velocity beneath the main line is the slowest. The slow velocity at the surface corresponds to the Hefei Basin (up to 7 km thick; e.g., Okay & Şengör, 1992) and the Lower Yangtze Basin. The mid-crust is slightly faster than the CJF-MTF systems (Feature 3) but slower than the regional crustal average velocity (black line in Figure 7). In the lower crust, there is a gentle ramp-shape fast-velocity structure that slightly dips southeast beneath the TLF (Feature 4). The structure starts at roughly ~20 km depth beneath the Hefei Basin (~32.5°N) and reaches the deepest around ~30 km depth across the TLF (~33.3°N; beneath station ST14). Parallel to the main line, the slow-velocity mid-crust beneath the TLF was modeled in an active-source wide angle reflection study which is ~100 km east of our main line (Xu et al., 2014; Figure S6d). In the mid-crust to lower crust, receiver function common-conversion-point (CCP) images (Zheng et al., 2014; Zhang, Lü, et al., 2019) also show a similar southwest gently dipping positive velocity gradient (Figure 8e), which spatially follows the top of the fast velocity ramp (Feature 4; Figure 5a) in the lower crust. We therefore consider Feature 4 robust, even though at this depth the model errors are larger than that of the other velocity features.

4.5. Feature 5—Fast-Velocity Mid-Crust to Lower Crust in the Dabie-Sulu Orogen

The two auxiliary lines sample the Dabie-Sulu Orogenic belt, which is famous for (ultra-) high-pressure (UHP) metamorphic rocks. The UHP rocks formed during the northward continental subduction of the SCB beneath the NCB (e.g., Zheng et al., 2003; Zheng et al., 2019), where the SCB crust subducted to lithospheric depth and then exhumed to surface. The crust underneath both orogens is in general high in velocity (Figures 6a and 6c), especially in the mid-crust to lower crust (Figures 7f–7h). Local ambient noise studies find a fast mid-crust to lower crust in the Northern Dabie complex (roughly beneath 30°N along the west profile) (Luo et al., 2012, 2018). An active-source study (Zhang, Deng, et al., 2013) indicates a fast P wave velocity in mid-crust to lower crust, especially under the Sulu Orogen. High values of bulk crustal V_p/V_s ratios are reported in receiver function studies in the orogens (He et al., 2014; Li et al., 2018). These observations in the orogen crust correspond well with the presence of abundant eclogite-facies rocks (e.g., Okay & Şengör, 1992; Zheng et al., 2003) and widespread postcollisional mafic igneous rocks due to the collapse of the orogen (e.g., Xu et al., 2016; Zhao, Dai, et al., 2013). An negative Bouguer gravity anomaly (Xu et al., 2016) also favors the presence of dense mafic crustal rocks (Christensen, & Mooney, 1995).

5. Crustal Thrust Faults and Lithospheric Wedges—Deformation of the Continental Collision

Our high-resolution crustal V_s model shows a highly heterogeneous crust underneath the array. Differences in crustal velocity domains spatially correlate well with the surface geology, suggesting many of the surface geological features are deep-seated. We are especially interested in and therefore focus below on seismic

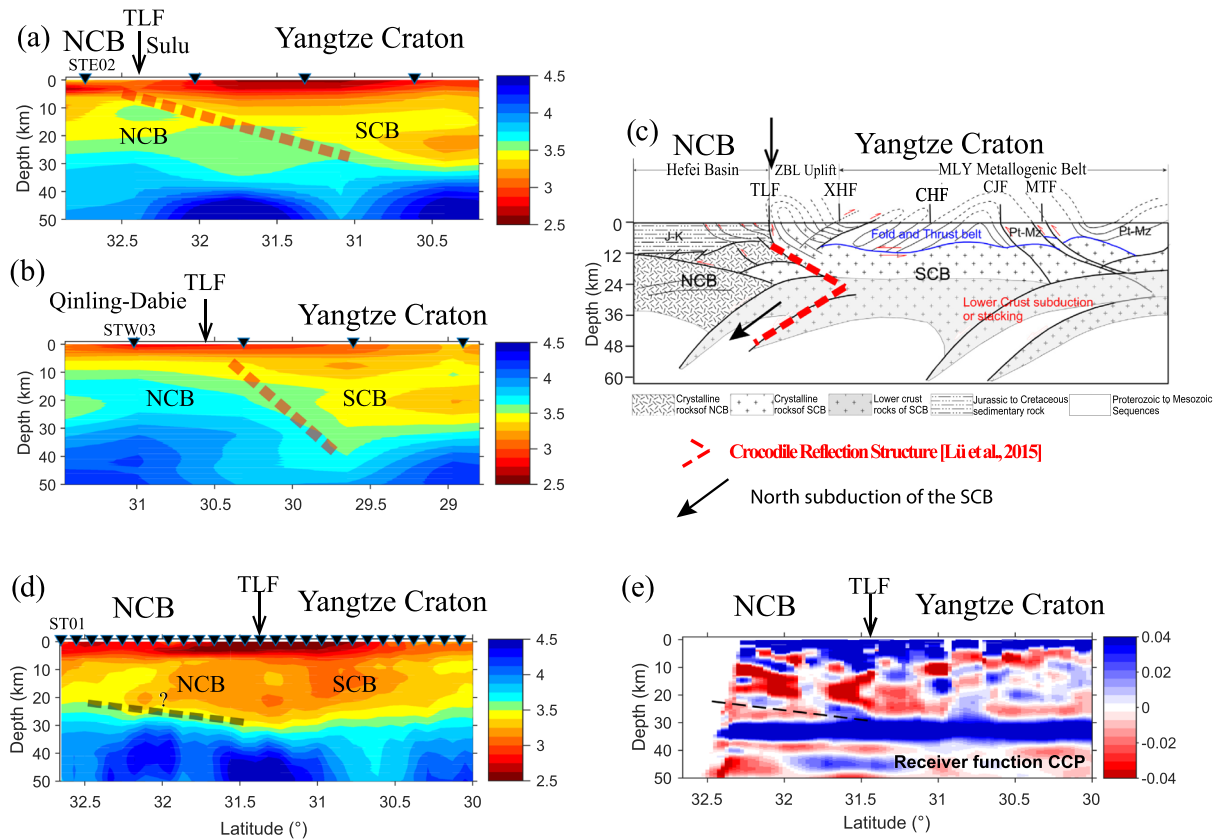


Figure 8. Crustal tectonic crocodile pattern along the Tanlu fault: (a) and (b), annotated Vs model for the east and west lines. Dashed lines approximate the velocity boundaries between the fast-velocity orogenic crust and the slow-velocity Yangtze crust, with an estimated length of ~191 km and ~120 km in the Sulu and Dabie Orogens, respectively; (c) the crocodile reflection pattern interpreted in the active-source reflection study of Lü et al. (2015); (d) and (e) Vs and receiver function CCP (relative amplitude with respect to direct *P* wave; Zheng et al., 2014) models along the main line. Note beneath the central line the fast-velocity orogenic mid-crust to lower crust seen in (a) and (b) is missing.

features that may have resulted from the Paleo-Tethys Ocean closure during the Triassic northward subduction of the SCB beneath the NCB.

5.1. South-Dipping Crustal Thrust Faults

Along the Dabie-Sulu orogenic belt, the fast velocity mid-crust to lower crust shown in the two auxiliary lines (Figures 6a and 6c) is interpreted as an orogenic feature, which is consistent with other geophysical models (section 4.5). Along the East line (Figure 8a), this fast velocity feature forms a long crustal scale fast-velocity ramp that extends over ~190 km to the south of the TLF. The top boundary of this feature defines a dipping crustal interface that separates the slow-velocity crust on top (dashed line in Figure 8a). Subparallel to the East line, an active-source deep profiling study proposed a crustal “crocodile” reflection pattern beneath the Tanlu Fault (Figure 8c; blue line (4) in Figure 1b). Such a tectonic “crocodile” reflection pattern is commonly ascribed to crustal thrust faults formed during continental collisions which accommodate deformation of colliding plates (Meissner, 1989; Snyder, 2002; Snyder & Goleby, 2016). Here such a south-dipping boundary inferred from the Vs model may simply mark the upper branch of the tectonic crocodile, that is, a major thrust fault (Figures 8a and 8b) that separated the NCB and SCB crust.

The tectonic origin of this crustal-scale thrust fault is debated. Lü et al. (2015) proposed a postorogenic formation due to intracontinental orogenies in response to the Paleo-Pacific subduction. Based on aeromagnetic anomalies, seismic reflection data, and other geotectonic records along the Dabie-Sulu orogenic belt, Li (1994, 1998) proposed a crustal detachment model for the Mesozoic continental collisional process east of the TLF, in which the crustal deformation due to the collision of the SCB with the NCB is kinematically different between the Sulu and Dabie orogens. In the Dabie Orogen, the crustal deformation is characterized

by a series of south-verging thrusts, which merged together into a steep fault zone near the northern margin of the orogen. In the Sulu Orogen, on the other hand, the deformation is more distributed, and a large-scale mid-crustal thrust zone is proposed between a northward obducting Yangtze upper crust and the lower crust and mantle lithosphere of the NCB over hundreds of kilometers (see Figure 3 of Li, 1994). Such a crustal detachment model for continental collision, also called flake tectonics (Oxburgh, 1972), often occurs when a promontory of one continent collides into another continent (Li, 1994, 1998; Oxburgh, 1972). The crustal Vs images (Figures 8a and 8b) here favor such a model, in which the southdipping fault separates the fast-velocity lower crust of the NCB from the slow-velocity SCB (Figures 8a and 8b).

Beneath the West line, the Tanlu Fault cuts diagonally across the eastern edge of the Dabie Orogen (Figure 1b). The steep south dipping boundary presented in the crustal shear-wave velocity model (Figure 8b) may not be representative of the localized deformations proposed in Li (1998). A high-resolution local ambient noise study in the eastern Dabie Orogen, on the other hand, shows a sharp, nearly vertical termination of the fast crustal velocity of the east Dabie Orogenic crust at its southern boundary (see Figure 8 in Luo et al., 2018). This is a clear image of a much localized deformation pattern proposed for the Dabie Orogen (Li, 1994, 1998).

5.2. North-Dipping NCB Lithospheric Wedges

A recent high-resolution regional surface-wave tomographic model (Bao et al., 2015) shows that different high velocity lithospheric blocks are present beneath the three lines (Figure 9). These high velocity features are interpreted as the present-time lithosphere of the NCB and SCB, accordingly. The lithospheric boundary between the NCB and the Yangtze Block is quite visible near the Tanlu Fault. At the bottom of the NCB lithosphere a north dipping negative-velocity gradient interface may be clearly drawn (black thick dashed lines in Figures 9a and 9b), which is interpreted as the lithosphere-asthenosphere-boundary of the NCB lithosphere. We tentatively interpret this boundary as the subduction interface between the NCB and SCB, which mimics the lower boundary of a tectonic wedge (Snyder, 2002).

A tectonic wedge may form during a continental collision, the rheologically stronger plate, for example the Archean NCB lithosphere, not yet disturbed by the Paleo-Pacific subduction, may exert less deformation, and thus splits the crust and subcrustal lithosphere of the younger and weaker converging plate, in this case the Yangtze plate. The tomographic models here thus define such a tectonic wedge (Figure 9) where the crust and subcrustal lithosphere of the NCB extrude into that of the SCB. Figure 9 further shows that the southward extension of the NCB lithosphere is different among the three lines: for example, beneath East line reaching over 100 km south of the TLF to $\sim 32^{\circ}\text{N}$ in the Sulu Orogen; beneath the West line ~ 50 km south of the TLF ($\sim 30.5^{\circ}\text{N}$) in the Dabie Orogen, and beneath the main line stopping near the TLF ($\sim 31.5^{\circ}\text{N}$). We note that the spatial termination of the NCB lithosphere in the Sulu Orogen spatially follows the Yangtze Fault (CJF) at surface, which spatially correlates with the linear magnetic low anomaly used in Li (1994) to mark the subduction front between the NCB and SCB.

5.3. Role of the Tanlu Fault

It is widely accepted that the Sulu orogenic belt is the eastward continuation of the Qinling-Dabie orogen, offset by the younger left-lateral Tanlu Fault (Li, 1998; Xu et al., 1987). The tectonic origin of the TLF offset is debated with numerous models being proposed, including a transform fault separating oppositely thrusting Dabie and Sulu orogens (Okay & Şengör, 1992), an indented boundary between the NCB and SCB (Yin & Nie, 1993), a rotated suture between the NCB and SCB/Yangtze (Gilder et al., 1999), and an indentation induced continent-tearing model (Li, 1994, 1998; Zhao et al., 2016). The crustal thrust faults and the lithospheric wedge inferred from tomographic models certainly favor the flake tectonics model in which the early TLF was mainly a tear fault due to the different orogenic kinematics across the TLF. Noteworthy is that the fast velocity mid-crust to lower crust present in both the Dabie and Sulu Orogens (Figures 8a and 8b) is missing beneath the main line (Figure 8c). This clearly shows that the TLF offset expressed at surface is also a whole-crust velocity feature and further implies that the offset may be spatially confined between the auxiliary lines, that is, less than 200 km.

5.4. Northward Subduction and Closure of Paleo-Tethys

The SCB and NCB continental collision has been traditionally considered as the northward subduction of the SCB lithosphere underneath the NCB, although recent models also proposed an opposite polarity, that

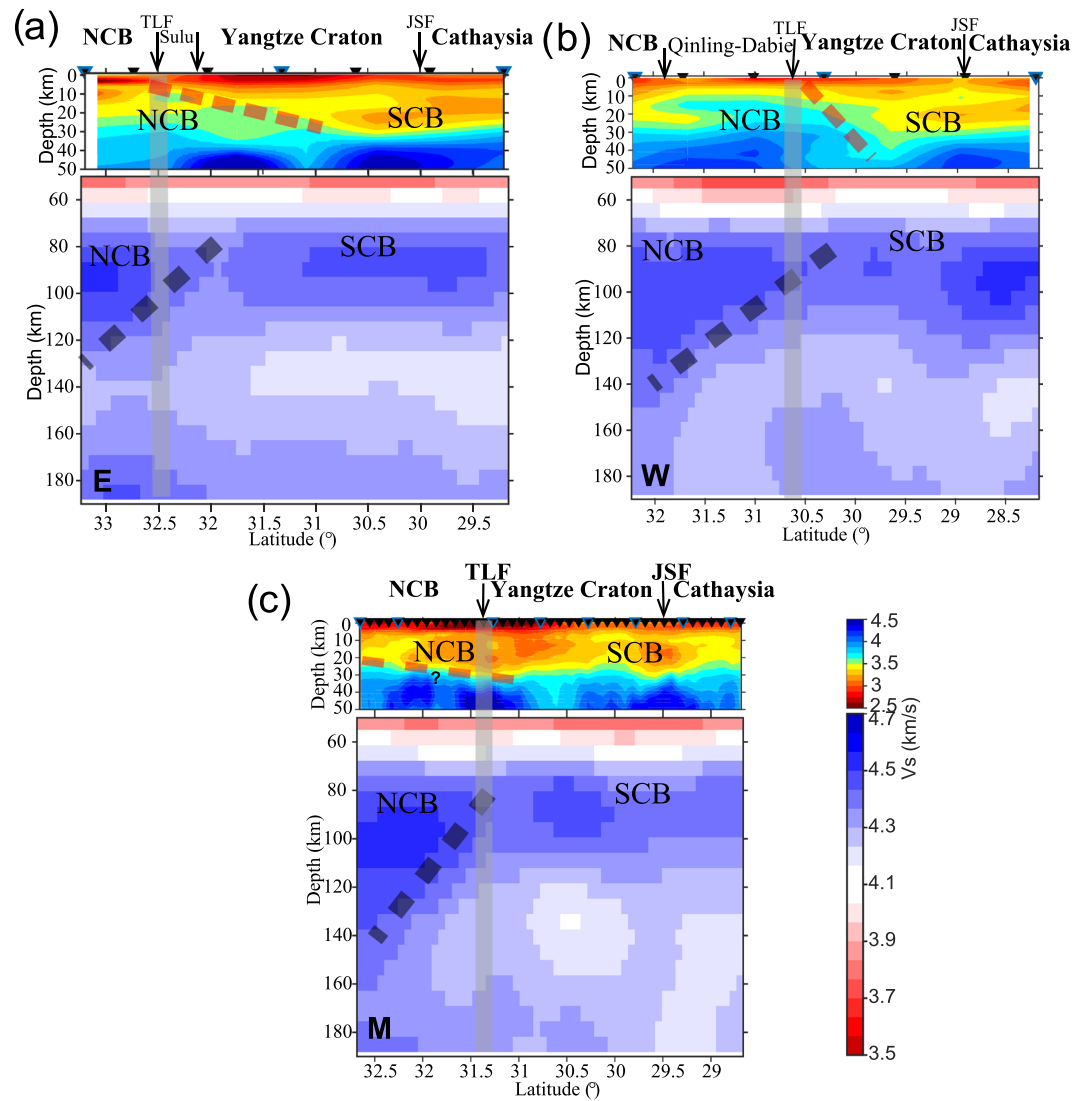


Figure 9. Tectonic wedges inferred from both the crust Vs model and the earthquake surface wave Vs model (Bao et al., 2015), indicated by the thick dashed lines. The vertical gray line shows the surface location of the Tanlu Fault. (a), (b), and (c) show the results of the east, west and main lines, respectively. Note the extrusion of the NCB lithosphere beneath the Yangtze crust, especially beneath the east line.

is, the NCB lithosphere was subducted southwards beneath the SCB (e.g., see discussion in Zheng et al., 2019). In the tectonic wedge model (Figure 9), the crust of the younger Yangtze lithosphere was overthrust northward above the mid-crust and lower crust of the NCB, as already seen in the Dabie-Sulu Orogen (Figure 8b); while the Yangtze subcrustal lithosphere was subducted northward beneath the NCB lithosphere. The tectonic wedge model presented in Figure 9 therefore provides a clear lithospheric scale image of the northward subduction of the SCB lithosphere beneath the NCB.

The subducted SCB lithosphere is however missing from the tomographic images (Figure 9). This may be attributed to the breakoff and subsequent detachment of the subducted SCB slab (e.g., Zheng et al., 2006) after the continental collision halted. Tomographic images (e.g., Deng et al., 2019; Shan et al., 2016) show that the SCB lithosphere has been further reworked, in response to various postcollisional extensional processes related to (paleo-) Pacific subduction or asthenospheric upwellings (e.g., Li et al., 2013; Li & Li, 2007; Wang et al., 2003; Zheng et al., 2006), leading to the thin (<100 km) and nonuniformly distributed SCB lithosphere (Figures 9b and 9c). We conclude that postcollisional reworking has significantly altered the regional

lithosphere; however, the lithospheric scars, in this case, the tectonic wedge formed during the closure of the Paleo-Tethys Ocean are still preserved in the lithospheric mantle.

6. Conclusions

Using waveform data from a dense array in south-east China, we obtained a high-resolution crustal shear-wave velocity model that gives very detailed structures of this portion of the Tethys tectonic domain. Combining available geophysical models, we recognize several remarkable seismic features that may be related to the Tethys tectonic evolution, especially during the final collision of the NCB with the SCB. Domains of crustal velocities are identified, which may be characteristic of local geological features, including the normal Precambrian crust, slow velocity major fault systems and suture zones, and fast velocity Dabie-Sulu Orogenic belt. The offset caused by the left-lateral TLF to the orogenic belt is clearly present in the whole crust velocity structure, which is confined spatially in between our two auxiliary seismic lines, that is, less than 200 km. In the Dabie-Sulu orogenic belt, a prominent south-dipping crustal velocity boundary is present, illustrating a well-reserved crustal thrust fault system. This system is interpreted as the boundary separating the overthrust SCB shallow and mid-crust on top of the NCB crust, which occurred during the SCB to NCB continental collision. Crustal deformation associated with the overthrust fault system is localized (~120 km) in the Dabie Orogen, but extends nearly ~200 km in the Sulu Orogen. Lithospheric wedges associated with the NCB extruded south underneath the SCB crust. Taken together, the crustal thrust faults and lithospheric wedges favor a northward subduction of the SCB underneath the NCB lithosphere in the continental collision after the closure of the Paleo-Tethys Ocean. Our study illustrates that high-resolution seismic imaging is a powerful tool to provide new and deep constraints regarding lithosphere deformation dynamics.

Data Availability Statement

Seismic data are provided by Seismic Array Laboratory, Institute of Geology and Geophysics, Chinese Academy of Sciences (doi:10.12129/IGGSL.Data.Observation/). The NCISP-8 data are openly available by sending request to the Institute. The stacked cross-correlation functions used for the tomographic inversions are stored at an open-source website—OSF: <http://osf.io/4ubpg>.

Acknowledgments

This project was partially supported by NSFC grants 91955210, 41625016, 41888101, 91755000, Y201715; and CAS program GJHZ1776. Thomas Bodin is funded by the European Union's Horizon 2020 research and innovation programme under grant agreement 716542. We are grateful to Tianyu Zheng, Haijiang Zhang, Rizheng He, Xuewei Bao, Kai Tao, and Weijia Sun for sharing their velocity models. This work was supported by resources provided by the Pawsey Supercomputing Centre with funding from the Australian Government and the Government of Western Australia. This is contribution 1511 from the ARC Centre of Excellence for Core to Crust Fluid Systems (<http://www.cfs.mq.edu.au>).

References

- Bao, X., Song, X., & Li, J. (2015). High-resolution lithospheric structure beneath mainland China from ambient noise and earthquake surface-wave tomography. *Earth and Planetary Science Letters*, *417*, 132–141. <https://doi.org/10.1016/j.epsl.2015.02.024>
- Bensen, G. D., Ritzwoller, M. H., Barmin, M. P., Levshin, A. L., Lin, F., Moschetti, M. P., et al. (2007). Processing seismic ambient noise data to obtain reliable broad-band surface wave dispersion measurements. *Geophysical Journal International*, *169*(3), 1239–1260. <https://doi.org/10.1111/j.1365-246X.2007.03374.x>
- Bodin, T., & Sambridge, M. (2009). Seismic tomography with the reversible jump algorithm. *Geophysical Journal International*, *178*(3), 1411–1436. <https://doi.org/10.1111/j.1365-246X.2009.04226.x>
- Bodin, T., Sambridge, M., Rawlinson, N., & Arroucau, P. (2012). Transdimensional tomography with unknown data noise. *Geophysical Journal International*, *189*(3), 1536–1556. <https://doi.org/10.1111/j.1365-246X.2012.05414.x>
- Calò, M., Bodin, T., & Romanowicz, B. (2016). Layered structure in the upper mantle across North America from joint inversion of long and short period seismic data. *Earth and Planetary Science Letters*, *449*, 164–175. <https://doi.org/10.1016/j.epsl.2016.05.054>
- Campillo, M., & Paul, A. (2003). Long-range correlations in the diffuse seismic coda. *Science*, *299*(5606), 547–549. <https://doi.org/10.1126/science.1078551>
- Cawood, P. A., Kröner, A., Collins, W. J., Kusky, T. M., Mooney, W. D., & Windley, B. F. (2009). *Accretionary orogens through Earth history, Special Publications* (Vol. 318, pp. 1–36). London: Geological Society. <https://doi.org/10.1144/SP318.1>
- Cawood, P. A., Hawkesworth, C. J., Pisarevsky, S. A., Dhuime, B., Capitano, F. A., & Nebel, O. (2018). Geological archive of the onset of plate tectonics. *Philosophical Transactions of the Royal Society A: Mathematical, Physical and Engineering Sciences*, *376*, 20170405. <https://doi.org/10.1098/rsta.2017.0405>
- Chib, S., & Greenberg, E. (1995). Understanding the Metropolis-Hastings algorithm. *The American Statistician*, *49*(4), 327–335.
- Christensen, N. I., & Mooney, W. (1995). Seismic velocity structure and composition of the continental crust: A global view. *Journal of Geophysical Research*, *100*(B6), 9761–9788. <https://doi.org/10.1029/95JB00259>
- Christensen, N. I. (1996). Poisson's ratio and crustal seismology. *Journal of Geophysical Research*, *101*(B2), 3139–3156. <https://doi.org/10.1029/95JB03446>
- Clerc, C., Ringenbach, J.-C., Jolivet, L., & Ballard, J.-F. (2018). Rifted margins: Ductile deformation, boudinage, continentward-dipping normal faults and the role of the weak lower crust. *Gondwana Research*, *53*, 20–40. <https://doi.org/10.1016/j.gr.2017.04.030>
- Deng, Y., Li, J., Peng, T., Ma, Q., Song, X., Sun, X., et al. (2019). Lithospheric structure in the Cathaysia block (South China) and its implication for the late Mesozoic magmatism. *Physics of the Earth and Planetary Interiors*, *291*, 24–34. <https://doi.org/10.1016/j.pepi.2019.04.003>
- Efron, B., & Tibshirani, R. (1986). Bootstrap methods for standard errors, confidence intervals, and other measures of statistical accuracy. *Statistical Science*, *1*(1), 54–75. <https://doi.org/10.1214/ss/1177013815>

- Fang, H., Yao, H., Zhang, H., Huang, Y.-C., & van der Hilst, R. D. (2015). Direct inversion of surface wave dispersion for three-dimensional shallow crustal structure based on ray tracing: Methodology and application. *Geophysical Journal International*, 201(3), 1251–1263. <https://doi.org/10.1093/gji/ggv080>
- Gan, C., Wang, Y., Zhang, Y., & Chen, X. (2019). Late Jurassic magmatism in the interior South China Block and its implication. *Journal of the Geological Society*, 176(4), 737–754. <https://doi.org/10.1144/jgs2018-177>
- Gilder, S. A., Leloup, P. H., Courtillot, V., Chen, Y., Coe, R. S., Zhao, X., et al. (1999). Tectonic evolution of the Tancheng-Lujiang (Tan-Lu) fault via middle Triassic to early Cenozoic paleomagnetic data. *Journal of Geophysical Research*, 104(B7), 15,365–15,390. <https://doi.org/10.1029/1999JB900123>
- Guo, L., Gao, R., Shi, L., Huang, Z., & Ma, Y. (2019). Crustal thickness and Poisson's ratios of South China revealed from joint inversion of receiver function and gravity data. *Earth and Planetary Science Letters*, 510, 142–152. <https://doi.org/10.1016/j.epsl.2018.12.039>
- Hacker, B. R., Wallis, S. R., Ratschbacher, L., Grove, M., & Gehrels, G. (2006). High-temperature geochronology constraints on the tectonic history and architecture of the ultrahigh-pressure Dabie-Sulu Orogen. *Tectonics*, 25, TC5006. <https://doi.org/10.1029/2005TC001937>
- He, R., Shang, X., Yu, C., Zhang, H., & Van der Hilst, R. D. (2014). A unified map of Moho depth and Vp/Vs ratio of continental China by receiver function analysis. *Geophysical Journal International*, 199(3), 1910–1918. <https://doi.org/10.1093/gji/ggu365>
- Heron, P. J., Pysklywec, R. N., & Stephenson, R. (2016). Lasting mantle scars lead to perennial plate tectonics. *Nature Communications*, 7, 11834. <https://doi.org/10.1038/ncomms11834>
- Jiang, G., Hu, S., Shi, Y., Zhang, C., Wang, Z., & Hu, D. (2019). Terrestrial heat flow of continental China: Updated dataset and tectonic implications. *Tectonophysics*, 753, 36–48. <https://doi.org/10.1016/j.tecto.2019.01.006>
- Jones, A. G. (2013). Imaging and observing the electrical Moho. *Tectonophysics*, 609, 423–436. <https://doi.org/10.1016/j.tecto.2013.02.025>
- Jones, A. G., & Ferguson, I. J. (2001). The electric Moho. *Nature*, 409(6818), 331–333. <https://doi.org/10.1038/35053053>
- Levshin, A. L., Pisarenko, V., & Pogrebinsky, G. (1972). On a frequency-time analysis of oscillations. Paper presented at Annales de Geophysique, Centre National de la Recherche Scientifique.
- Li, H., Song, X., Lü, Q., Yang, X., Deng, Y., Ouyang, L., et al. (2018). Seismic imaging of lithosphere structure and upper mantle deformation beneath east-Central China and their tectonic implications. *Journal of Geophysical Research: Solid Earth*, 123, 2856–2870. <https://doi.org/10.1002/2017JB014992>
- Li, X.-H., Li, W.-X., Li, Z.-X., Lo, C.-H., Wang, J., Ye, M.-F., & Yang, Y.-H. (2009). Amalgamation between the Yangtze and Cathaysia blocks in South China: Constraints from SHRIMP U–Pb zircon ages, geochemistry and Nd–Hf isotopes of the Shuangxiwu volcanic rocks. *Precambrian Research*, 174(1–2), 117–128. <https://doi.org/10.1016/j.precamres.2009.07.004>
- Li, X.-H., Li, Z.-X., Li, W.-X., Wang, X.-C., & Gao, Y. (2013). Revisiting the “C-type adakites” of the lower Yangtze River belt, central eastern China: In-situ zircon Hf–O isotope and geochemical constraints. *Chemical Geology*, 345, 1–15. <https://doi.org/10.1016/j.chemgeo.2013.02.024>
- Li, X., Zhu, P., Kusky, T. M., Gu, Y., Peng, S., Yuan, Y., & Fu, J. (2015). Has the Yangtze craton lost its roof? A comparison between the North China and Yangtze cratons. *Tectonophysics*, 655, 1–14. <https://doi.org/10.1016/j.tecto.2015.04.008>
- Li, Z.-X. (1994). Collision between the north and South China blocks: A crustal-detachment model for suturing in the region east of the Tanlu fault. *Geology*, 22(8), 739–742. [https://doi.org/10.1130/0091-7613\(1994\)022%3C0739:CBTNAS%3E2.3.CO;2](https://doi.org/10.1130/0091-7613(1994)022%3C0739:CBTNAS%3E2.3.CO;2)
- Li, Z.-X. (1998). Tectonic history of the major east Asian lithospheric blocks since the mid-Proterozoic—A synthesis. In M. J. Flower, S. L. Chung, C. H. Lo, & T. Y. Lee (Eds.), *Mantle Dynamics and Plate Interactions in East Asia* (pp. 221–243). Washington, DC, United States: American Geophysical Union. <https://doi.org/10.1029/GD027p0221>
- Li, Z.-X., Li, X., Kinny, P., & Wang, J. (1999). The breakup of Rodinia: Did it start with a mantle plume beneath South China? *Earth and Planetary Science Letters*, 173(3), 171–181. [https://doi.org/10.1016/S0012-821X\(99\)00240-X](https://doi.org/10.1016/S0012-821X(99)00240-X)
- Li, Z.-X., Li, X. H., Kinny, P. D., Wang, J., Zhang, S., & Zhou, H. (2003). Geochronology of Neoproterozoic syn-rift magmatism in the Yangtze Craton, South China and correlations with other continents: Evidence for a mantle superplume that broke up Rodinia. *Precambrian Research*, 122(1–4), 85–109. [https://doi.org/10.1016/S0301-9268\(02\)00208-5](https://doi.org/10.1016/S0301-9268(02)00208-5)
- Li, Z.-X., & Li, X.-H. (2007). Formation of the 1300-km-wide intracontinental orogen and postorogenic magmatic province in Mesozoic South China: A flat-slab subduction model. *Geology*, 35(2), 179–182. <https://doi.org/10.1130/G23193A1>
- Li, Z. X., Li, X. H., Wartho, J. A., Clark, C., Li, W. X., Zhang, C. L., & Bao, C. (2010). Magmatic and metamorphic events during the early Paleozoic Wuyi-Yunkai orogeny, southeastern South China: New age constraints and P–T conditions. *Geological Society of America Bulletin*, 122(5–6), 772–793. <https://doi.org/10.1130/B30021.1>
- Li, Z. X., Li, X. H., Li, W. X., & Ding, S. (2008). Was Cathaysia part of Proterozoic Laurentia? New data from Hainan Island, South China. *Terra Nova*, 20(2), 154–164. <https://doi.org/10.1111/j.1365-3121.2008.00802.x>
- Lin, F.-C., Li, D., Clayton, R. W., & Hollis, D. (2013). High-resolution 3D shallow crustal structure in Long Beach, California: Application of ambient noise tomography on a dense seismic array. *Geophysics*, 78(4), Q45–Q56. <https://doi.org/10.1190/geo2012-0453.1>
- Liu, D. Y., Nutman, A. P., Compston, W., Wu, J. S., & Shen, Q. H. (1992). Remnants of ≥ 3800 Ma crust in the Chinese part of the Sino-Korean craton. *Geology*, 20(4), 339–342. [https://doi.org/10.1130/0091-7613\(1992\)020%3C0339:ROMCIT%3E2.3.CO;2](https://doi.org/10.1130/0091-7613(1992)020%3C0339:ROMCIT%3E2.3.CO;2)
- Lü, Q., Shi, D., Liu, Z., Zhang, Y., Dong, S., & Zhao, J. (2015). Crustal structure and geodynamics of the middle and lower reaches of Yangtze metallogenic belt and neighboring areas: Insights from deep seismic reflection profiling. *Journal of Asian Earth Sciences*, 114, 704–716. <https://doi.org/10.1016/j.jseas.2015.03.022>
- Luo, S., Yao, H., Li, Q., Wang, W., Wan, K., Meng, Y., & Liu, B. (2019). High-resolution 3D crustal S-wave velocity structure of the middle-lower Yangtze River Metallogenic Belt and implications for its deep geodynamic setting. *Science China Earth Sciences*, 62, 1361–1378. <https://doi.org/10.1007/s11430-018-9352-9>
- Luo, Y., Xu, Y., & Yang, Y. (2012). Crustal structure beneath the Dabie orogenic belt from ambient noise tomography. *Earth and Planetary Science Letters*, 313–314, 12–22. <https://doi.org/10.1016/j.epsl.2011.11.004>
- Luo, Y., Zhao, K., Tang, C.-C., & Xu, Y. (2018). Seismic evidence for multiple-stage exhumation of high/ultrahigh pressure metamorphic rocks in the eastern Dabie orogenic belt. *Geophysical Journal International*, 214(2), 1379–1390. <https://doi.org/10.1093/gji/ggy208>
- Meissner, R. (1989). Rupture, creep, lamellae and crocodiles: Happenings in the continental crust. *Terra Nova*, 1(1), 17–28. <https://doi.org/10.1111/j.1365-3121.1989.tb00321.x>
- Meng, Q.-R., & Zhang, G.-W. (2000). Geologic framework and tectonic evolution of the Qinling orogen, Central China. *Tectonophysics*, 323(3–4), 183–196. [https://doi.org/10.1016/S0040-1951\(00\)00106-2](https://doi.org/10.1016/S0040-1951(00)00106-2)
- Menzies, M. A., & Xu, Y. (1998). Geodynamics of the North China craton. M. F. J. Flower, S.-L. Chung, C.-H. Lo, & T.-Y. Lee (Eds.), *Mantle dynamics and plate interactions in East Asia* (Vol. 27, pp. 155–165). Washington, DC: American Geophysical Union. <https://doi.org/10.1029/GD027p0155>
- Metcalf, I. (2013). Gondwana dispersion and Asian accretion: Tectonic and palaeogeographic evolution of eastern Tethys. *Journal of Asian Earth Sciences*, 66, 1–33. <https://doi.org/10.1016/j.jseas.2012.12.020>

- Okay, A. I., & Şengör, C. A. M. (1992). Evidence for intracontinental thrust-related exhumation of the ultra-high-pressure rocks in China. *Geology*, 20(5), 411–414. [https://doi.org/10.1130/0091-7613\(1992\)020%3C0411:EFITRE%3E2.3.CO;2](https://doi.org/10.1130/0091-7613(1992)020%3C0411:EFITRE%3E2.3.CO;2)
- Oxburgh, E. R. (1972). Flake tectonics and continental collision. *Nature*, 239(5369), 202–204. <https://doi.org/10.1038/239202a0>
- Peron-Pinvidic, G., Manatschal, G., & the “IMAGinING RIFTING” Workshop Participants (2019). Rifted margins: State of the art and future challenges. *Frontiers in Earth Science*, 7(218). <https://doi.org/10.3389/feart.2019.00218>
- Rawlinson, N., & Sambridge, M. (2005). The fast marching method: An effective tool for tomographic imaging and tracking multiple phases in complex layered media. *Exploration Geophysics*, 36(4), 341–350. <https://doi.org/10.1071/EG05341>
- Şengör, A. M. (1990). Plate tectonics and orogenic research after 25 years: A Tethyan perspective. *Earth-Science Reviews*, 187(1-3), 315–344. [https://doi.org/10.1016/0040-1951\(91\)90427-T](https://doi.org/10.1016/0040-1951(91)90427-T)
- Sengor, A. M. C., Natal'in, B. A., & Burtman, V. S. (1993). Evolution of the Altaid tectonic collage and Palaeozoic crustal growth in Eurasia. *Nature*, 364(6435), 299–307. <https://doi.org/10.1038/364299a0>
- Shan, B., Xiong, X., Zhao, K. F., Xie, Z. J., Zheng, Y., & Zhou, L. (2016). Crustal and upper-mantle structure of South China from Rayleigh wave tomography. *Geophysical Journal International*, 208(3), 1643–1654.
- Shapiro, N. M., & Campillo, M. (2004). Emergence of broadband Rayleigh waves from correlations of the ambient seismic noise. *Geophysical Research Letters*, 31, L07614. <https://doi.org/10.1029/2004GL019491>
- Snyder, D. B. (2002). Lithospheric growth at margins of cratons. *Tectonophysics*, 355(1–4), 7–22. [https://doi.org/10.1016/S0040-1951\(02\)00131-2](https://doi.org/10.1016/S0040-1951(02)00131-2)
- Snyder, D. B., & Goley, B. R. (2016). Seismic reflection patterns associated with continental convergent margins through time. *Tectonophysics*, 692, 3–13. <https://doi.org/10.1016/j.tecto.2016.04.027>
- Stachnik, J. C., Dueker, K., Schutt, D. L., & Yuan, H. (2008). Imaging Yellowstone plume-lithosphere interactions from inversion of ballistic and diffusive Rayleigh wave dispersion and crustal thickness data. *Geochemistry, Geophysics, Geosystems*, 9, Q06004. <https://doi.org/10.1029/2008GC001992>
- Stampfli, G. M., Hochard, C., Vêrard, C., Wilhem, C., & vonRaumer, J. (2013). The formation of Pangea. *Tectonophysics*, 593, 1–19. <https://doi.org/10.1016/j.tecto.2013.02.037>
- Stern, R. J., Li, S.-M., & Randy Keller, G. (2018). Continental crust of China: A brief guide for the perplexed. *Earth-Science Reviews*, 179, 72–94. <https://doi.org/10.1016/j.earscirev.2018.01.020>
- Thybo, H., & Artemieva, I. M. (2013). Moho and magmatic underplating in continental lithosphere. *Tectonophysics*, 609, 605–619. <https://doi.org/10.1016/j.tecto.2013.05.032>
- van der Velden, A. J., & Cook, F. A. (2005). Relict subduction zones in Canada. *Journal of Geophysical Research*, 110, B08403. <https://doi.org/10.1029/2004JB003333>
- Wan, B., Li, S., Xiao, W., & Windley, B. F. (2018). Where and when did the Paleo-Asian ocean form? *Precambrian Research*, 317, 241–252. <https://doi.org/10.1016/j.precamres.2018.09.003>
- Wan, B., Wu, F., Chen, L., Zhao, L., Liang, X., Xiao, W., & Zhu, R. (2019). Cyclical one-way continental rupture-drift in the Tethyan evolution: Subduction-driven plate tectonics. *Science China Earth Sciences*, 62(12), 2005–2016. <https://doi.org/10.1007/s11430-019-9393-4>
- Wang, Q., Bagdassarov, N., & Ji, S. (2013). The Moho as a transition zone: A revisit from seismic and electrical properties of minerals and rocks. *Tectonophysics*, 609, 395–422. <https://doi.org/10.1016/j.tecto.2013.08.041>
- Wang, Y., Fan, W., Zhang, G., & Zhang, Y. (2013). Phanerozoic tectonics of the South China block: Key observations and controversies. *Gondwana Research*, 23(4), 1273–1305. <https://doi.org/10.1016/j.gr.2012.02.019>
- Wang, Y., Fan, W., Guo, F., Peng, T., & Li, C. (2003). Geochemistry of Mesozoic mafic rocks adjacent to the Chenzhou-Linwu fault, South China: Implications for the lithospheric boundary between the Yangtze and Cathaysia blocks. *International Geology Review*, 45(3), 263–286. <https://doi.org/10.2747/0020-6814.45.3.263>
- Wu, F.-Y., Lin, J.-Q., Wilde, S. A., Zhang, X. O., & Yang, J.-H. (2005). Nature and significance of the early cretaceous giant igneous event in eastern China. *Earth and Planetary Science Letters*, 233(1-2), 103–119. <https://doi.org/10.1016/j.epsl.2005.02.019>
- Wu, F.-Y., Yang, J.-H., Xu, Y.-G., Wilde, S. A., & Walker, R. J. (2019). Destruction of the North China craton in the Mesozoic. *Annual Review of Earth and Planetary Sciences*, 47(1), 173–195. <https://doi.org/10.1146/annurev-earth-053018-060342>
- Wu, S., Jiang, M., He, Y., Zhao, L., & Ai, Y. (2018). NW-SE structural contrast of shear wave velocity and radial anisotropy beneath the Hefei-Jinhua seismic profile derived from ambient noise tomography. *Chinese Journal of Geophysics (in Chinese)*, 61(2), 584–592. <https://doi.org/10.6038/cjg201810261>
- Xiao, W., Windley, B. F., Allen, M. B., & Han, C. (2013). Paleozoic multiple accretionary and collisional tectonics of the Chinese Tianshan orogenic collage. *Gondwana Research*, 23(4), 1316–1341. <https://doi.org/10.1016/j.gr.2012.01.012>
- Xin, H., Zhang, H., Kang, M., He, R., Gao, L., & Gao, J. (2018). High-resolution lithospheric velocity structure of continental China by double-difference seismic travel-time tomography. *Seismological Research Letters*, 90(1), 229–241.
- Xu, T., Zhang, Z., Tian, X., Liu, B., Bai, Z., Lü, Q., & Teng, J. (2014). Crustal structure beneath the middle-lower Yangtze metallogenic belt and its surrounding areas: Constraints from active source seismic experiment along the Lixin to Yixing profile in East China. *Acta Petrologica Sinica*, 30(4), 918–930.
- Xu, J., Zhu, G., Tong, W., Cui, K., & Liu, Q. (1987a). Formation and evolution of the Tancheng-Lujiang wrench fault system: A major shear system to the northwest of the Pacific Ocean. *Tectonophysics*, 134(4), 273–310. [https://doi.org/10.1016/0040-1951\(87\)90342-8](https://doi.org/10.1016/0040-1951(87)90342-8)
- Xu, S., Su, W., Liu, Y., Jiang, L., Ji, S., Okay, A. I., & Şengör, A. M. C. (1992). Diamond from the Dabie Shan metamorphic rocks and its implication for tectonic setting. *Science*, 256(5053), 80–82.
- Xu, Y., Zhang, S., Griffin, W. L., Yang, Y., Yang, B., Luo, Y., et al. (2016). How did the Dabie Orogen collapse? Insights from 3-D magnetotelluric imaging of profile data. *Journal of Geophysical Research: Solid Earth*, 121, 5169–5185. <https://doi.org/10.1002/2015JB012717>
- Yang, Y., Ritzwoller, M. H., Zheng, Y., Shen, W., Levshin, A. L., & Xie, Z. (2012). A synoptic view of the distribution and connectivity of the mid-crustal low velocity zone beneath Tibet. *Journal of Geophysical Research*, 117, B04303. <https://doi.org/10.1029/2011JB008810>
- Yao, H., van Der Hilst, R. D., & de Hoop, M. V. (2006). Surface-wave array tomography in SE Tibet from ambient seismic noise and two-station analysis—I. Phase velocity maps. *Geophysical Journal International*, 166(2), 732–744. <https://doi.org/10.1111/j.1365-246X.2006.03028.x>
- Yin, A., & Nie, S. (1993). An indentation model for the north and South China collision and the development of the tan-Lu and Honam fault systems, eastern Asia. *Tectonics*, 12(4), 801–813. <https://doi.org/10.1029/93TC00313>
- Young, M. K., Rawlinson, N., & Bodin, T. (2013). Transdimensional inversion of ambient seismic noise for 3D shear velocity structure of the Tasmanian crust. *Geophysics*, 78(3), WB49–WB62. <https://doi.org/10.1190/geo2012-0356.1>

- Yu, J.-H., Wang, L., O'Reilly, S. Y., Griffin, W., Zhang, M., Li, C., & Shu, L. (2009). A Paleoproterozoic orogeny recorded in a long-lived cratonic remnant (Wuyishan terrane), eastern Cathaysia Block, China. *Precambrian Research*, *174*(3-4), 347–363. <https://doi.org/10.1016/j.precamres.2009.08.009>
- Yuan, H., & Bodin, T. (2018). A probabilistic shear wave velocity model of the crust in the central west Australian Craton constrained by transdimensional inversion of ambient noise dispersion. *Tectonics*, *37*, 1994–2012. <https://doi.org/10.1029/2017TC004834>
- Zhang, K., Lü, Q., Yan, J., Shao, L., Guo, D., & Zhang, Y. (2019). The subduction and continental collision of the North China and Yangtze blocks: Magnetotelluric evidence from the Susong-Anqing section of Western Anhui, China. *Geophysical Journal International*, *216*(3), 2114–2128. <https://doi.org/10.1093/gji/ggy541>
- Zhang, L., Jin, S., Wei, W., Ye, G., Jing, J., Dong, H., & Xie, C. (2015). Lithospheric electrical structure of South China imaged by magnetotelluric data and its tectonic implications. *Journal of Asian Earth Sciences*, *98*, 178–187. <https://doi.org/10.1016/j.jseas.2014.10.034>
- Zhang, X., Curtis, A., Galetti, E., & de Ridder, S. (2018). 3-D Monte Carlo surface wave tomography. *Geophysical Journal International*, *215*(3), 1644–1658. <https://doi.org/10.1093/gji/ggy362>
- Zhang, Z., Badal, J., Li, Y., Chen, Y., Yang, L., & Teng, J. (2005). Crust–upper mantle seismic velocity structure across Southeastern China. *Tectonophysics*, *395*(1–2), 137–157. <https://doi.org/10.1016/j.tecto.2004.08.008>
- Zhang, Z., Deng, Y., Chen, L., Wu, J., Teng, J., & Panza, G. (2013). Seismic structure and rheology of the crust under mainland China. *Gondwana Research*, *23*(4), 1455–1483. <https://doi.org/10.1016/j.gr.2012.07.010>
- Zhang, Z., Xu, T., Zhao, B., & Badal, J. (2013). Systematic variations in seismic velocity and reflection in the crust of Cathaysia: New constraints on intraplate orogeny in the South China continent. *Gondwana Research*, *24*(3–4), 902–917. <https://doi.org/10.1016/j.gr.2012.05.018>
- Zhao, G., & Cawood, P. A. (2012). Precambrian geology of China. *Precambrian Research*, *222–223*, 13–54. <https://doi.org/10.1016/j.precamres.2012.09.017>
- Zhao, L., Allen, R. M., Zheng, T., & Zhu, R. (2012). High-resolution body wave tomography models of the upper mantle beneath eastern China and the adjacent areas. *Geochemistry, Geophysics, Geosystems*, *13*, Q06007. <https://doi.org/10.1029/2012GC004119>
- Zhao, G., Wang, Y., Huang, B., Dong, Y., Li, S., Zhang, G., & Yu, S. (2018). Geological reconstructions of the east Asian blocks: From the breakup of Rodinia to the assembly of Pangea. *Earth-Science Reviews*, *186*, 262–286. <https://doi.org/10.1016/j.earscirev.2018.10.003>
- Zhao, L., Malusà, M. G., Yuan, H., Paul, A., Guillot, S., Lu, Y., et al. (2020). Evidence for a serpentinized plate interface favouring continental subduction. *Nature Communications*, *11*, 2171. <https://doi.org/10.1038/s41467-020-15904-7>
- Zhao, L., Zheng, T., & Lu, G. (2013). Distinct upper mantle deformation of cratons in response to subduction: Constraints from SKS wave splitting measurements in eastern China. *Gondwana Research*, *23*(1), 39–53. <https://doi.org/10.1016/j.gr.2012.04.007>
- Zhao, T., Zhu, G., Lin, S., & Wang, H. (2016). Indentation-induced tearing of a subducting continent: Evidence from the tan–Lu fault zone, East China. *Earth-Science Reviews*, *152*, 14–36. <https://doi.org/10.1016/j.earscirev.2015.11.003>
- Zhao, Z.-F., Dai, L.-Q., & Zheng, Y.-F. (2013). Postcollisional mafic igneous rocks record crust-mantle interaction during continental deep subduction. *Scientific Reports*, *3*, 3413. <https://doi.org/10.1038/srep03413>
- Zheng, J., Griffin, W. L., O'Reilly, S. Y., Yang, J., Li, T., Zhang, M., et al. (2006). Mineral chemistry of Peridotites from Paleozoic, Mesozoic and Cenozoic lithosphere: Constraints on mantle evolution beneath eastern China. *Journal of Petrology*, *47*(11), 2233–2256. <https://doi.org/10.1093/ptrology/egl042>
- Zheng, J. P., Lee, C. T. A., Lu, J. G., Zhao, J. H., Wu, Y. B., Xia, B., et al. (2015). Refertilization-driven destabilization of subcontinental mantle and the importance of initial lithospheric thickness for the fate of continents. *Earth and Planetary Science Letters*, *409*, 225–231. <https://doi.org/10.1016/j.epsl.2014.10.042>
- Zheng, T.-Y., Zhao, L., He, Y.-M., & Zhu, R.-X. (2014). Seismic imaging of crustal reworking and lithospheric modification in eastern China. *Geophysical Journal International*, *196*(2), 656–670. <https://doi.org/10.1093/gji/ggt420>
- Zheng, Y.-F., Fu, B., Gong, B., & Li, L. (2003). Stable isotope geochemistry of ultrahigh pressure metamorphic rocks from the Dabie–Sulu orogen in China: Implications for geodynamics and fluid regime. *Earth-Science Reviews*, *62*(1–2), 105–161. [https://doi.org/10.1016/S0012-8252\(02\)00133-2](https://doi.org/10.1016/S0012-8252(02)00133-2)
- Zheng, Y.-F., Zhao, Z.-F., & Chen, R.-X. (2019). Ultrahigh-pressure metamorphic rocks in the Dabie-Sulu orogenic belt: Compositional inheritance and metamorphic modification. Special Publications, (Vol. 474, pp. 89–132). London: Geological Society. <https://doi.org/10.1144/SP474.9>
- Zheng, T., Duan, Y., Xu, W., & Ai, Y. (2017). A seismic model for crustal structure in North China Craton. *Earth and Planetary Physics*, *1*(1), 26–34. <https://doi.org/10.26464/epp2017004>
- Zheng, Y., Xiao, W., & Zhao, G. (2013). Introduction to tectonics of China. *Gondwana Research*, *23*(4), 1189–1206. <https://doi.org/10.1016/j.gr.2012.10.001>
- Zhou, L., Xie, J., Shen, W., Zheng, Y., Yang, Y., Shi, H., & Ritzwoller, M. H. (2012). The structure of the crust and uppermost mantle beneath South China from ambient noise and earthquake tomography. *Geophysical Journal International*, *189*(3), 1565–1583. <https://doi.org/10.1111/j.1365-246X.2012.05423.x>
- Zhu, R. X., Chen, L., Wu, F. Y., & Liu, J. L. (2011). Timing, scale and mechanism of the destruction of the North China Craton. *Science China Earth Sciences*, *54*(6), 789–797. <https://doi.org/10.1007/s11430-011-4203-4>
- Zhu, R., Xu, Y., Zhu, G., Zhang, H., Xia, Q., & Zheng, T. (2012). Destruction of the North China Craton. *Science China Earth Sciences*, *55*(10), 1565–1587. <https://doi.org/10.1007/s11430-012-4516-y>

References From the Supporting Information

- Sun, W., & Kennett, B. L. N. (2016). Uppermost mantle structure beneath eastern China and its surroundings from Pn and Sn tomography. *Geophysical Research Letters*, *43*, 3143–3149. <https://doi.org/10.1002/2016GL068618>
- Tao, K., Grand, S. P., & Niu, F. (2018). Seismic structure of the upper mantle beneath eastern Asia from full waveform seismic tomography, geochemistry, geophysics. *Geosystems*, *19*(8), 2732–2763.
- Yao, H., Xu, G., Xiao, X., & Zhu, L. (2004). A quick tracing method based on image analysis technique for the determination of dual stations phase velocities dispersion curve of surface wave [J]. *Seismological and Geomagnetic Observation and Research*, *25*, 1–8.
- Zhang, Y., Lü, Q., Teng, J., Wang, Q., & Xu, T. (2014). Discussion on the crustal density structure and deep mineralization background in the middle-lower Yangtze metallogenic belt and its surrounding areas: Constraints from the gravity inversion. *Acta Petrologica Sinica*, *30*(4), 931–940.